Research Paper

Ultrahigh-resolution optical coherence microscopy accurately classifies precancerous and cancerous human cervix free of labeling

Xianxu Zeng,[1,2,†] Xiaoan Zhang,[3,†] Canyu Li,[2,4] Xiaofang Wang,[2,5] Jason Jerwick,[2] Tao Xu,[2,6] Yuan Ning,[2,7] Yihong Wang,[8] Linlin Zhang,[5] Zhan Zhang,[5] Yutao Ma,[6] Chao Zhou,[2,9,10,✉]

1. Department of Pathology, the Third Affiliated Hospital of Zhengzhou University, Zhengzhou, 450052, China.
2. Department of Electrical and Computer Engineering, Lehigh University, Bethlehem PA 18015, USA.
3. Department of Imaging, the Third Affiliated Hospital, Zhengzhou University, Zhengzhou, 450052, China.
4. Department of Gynecology and Obstetrics, the Third Affiliated Hospital, Zhengzhou University, Zhengzhou 450052, China.
5. Department of Clinical Laboratory, the Third Affiliated Hospital, Zhengzhou University, Zhengzhou 450052, China.
6. State Key Laboratory of Software Engineering, Wuhan University, Wuhan 430072, China.
7. Department of Precision Instrument Engineering, Tianjin University, Tianjin 300072, China.
8. Department of Pathology and Laboratory Medicine, Rhode Island Hospital/Warren Alpert Medical School of Brown University, Rhode Island 02912, USA
9. Department of Bioengineering, Lehigh University, Bethlehem PA 18015, USA.
10. Center for Photonics and Nanoelectronics, Lehigh University, Bethlehem PA 18015, USA.

† These authors contributed equally to this work.

✉ Corresponding author: Prof. Chao Zhou, Department of Bioengineering, Department of Electrical and Computer Engineering, Lehigh University, Packard Laboratory Room 402, 19 Memorial Drive West, Bethlehem, PA 18015, USA, Tel: +1 (610)758-5092, Fax: +1 (610)758-6279, E-mail: chaozhou@lehigh.edu

Abstract

Cervical cancer remains the fourth most common cause of cancer worldwide and the third leading cause of cancer deaths for women in developing countries. Traditional screening tools, such as human papillomavirus and Pap tests, cannot provide results in real-time and cannot localize suspicious regions. Colposcopy-directed biopsies are invasive in nature and only a few sites of the cervix may be chosen for investigation. A non-invasive, label-free and real-time imaging method with a resolution approaching that of histopathology is desirable for early detection of the disease.

Methods: Ultrahigh-resolution optical coherence microscopy (OCM) is an emerging imaging technique used to obtain 3-dimensional (3-D) "optical biopsies" of biological samples with cellular resolution. In this study, 497 3-D OCM datasets from 159 specimens were collected from 92 patients.

Results: Distinctive patterns for normal cervix, squamocolumnar junction, ectropion, low-grade and high-grade squamous intraepithelial lesions (LSIL and HSIL) and invasive cervical lesions were clearly observed from OCM images, which matched well with corresponding histological slides. OCM images demonstrated a sensitivity of 80% (95% confidence interval, CI, 72%-86%) and a specificity of 89% (95% CI, 84%-93%) for detecting high-risk lesions (HSIL and invasive lesions) when blindly tested by three investigators. A substantial inter-observer agreement was observed (κ=0.627), which showed high diagnostic consistency among three investigators.

Conclusion: These results laid the foundation for future non-invasive optical evaluation of cervical tissue *in vivo*, which could lead to a less invasive and more effective screening and "see-and-treat" strategy for the management of cervical cancer.

Key words: cervical cancer, optical biopsy, optical coherence tomography (OCT), optical coherence microscopy (OCM), screening

Introduction

Cervical cancer is the fourth most common cancer in women worldwide with ~520,000 new cases and ~260,000 deaths per year. 87% of cervical cancer occurrences are in developing countries, where

cervical cancer is the third leading cause of cancer death for women. The mortality rate from cervical cancer in these developing countries can be as much as 18 times higher than that within developed countries [1-3]. Effective screening has decreased cervical cancer incidence by 70% for high-income countries [2]. With the widespread dissemination of cervical screening systems, the incidence of cervical cancer has decreased more than 50% in the United States in the past 30 years, but there still were 12,990 new cases of cervical cancer in the United States in 2016, with 4,120 deaths [4]. In contrast to decreasing incidence trends in developed countries, a substantial increase in both morbidity and mortality was seen in Zimbabwe, Central Asia and some countries of Central and Eastern Europe [5, 6]. In China, an increasing trend was also observed from 2000 to 2011 [7]. This may reflect the inadequacy of Papanicolaou (Pap) test screening in China, as only one-fifth of Chinese women have reported ever having a Pap test for cervical cancer screening [8], in contrast to over three-fourths of women in the United States [9].

Cervical cancer is preventable due to screening, with positive patient outlooks for early diagnosis [4, 10]. The anatomic visibility of ectocervix, the accessibility of cervical exfoliated cells and the development of screening techniques make cervical cytology screening feasible in high throughput settings [11]. High-risk human papillomavirus (HPV) is the leading cause of precancerous and cancerous cervical lesions. Early diagnosis and treatment of suspicious lesions is very successful because HPV infections have long intervals of progression to cancer [12]. Cytology testing in combination with the high risk HPV test constitutes the basic cervical cancer screening system [13]. Other testing methods such as visual inspection of cervix with acetic acid (VIA) and colposcopy have also been recommended by World Health Organization (WHO) [14].

Each screening technique has advantages and disadvantages. For example, HPV testing has a reported sensitivity of 95.2% and a specificity of 62.5% for detection of cervical intraepithelial neoplasia 2+ (CIN2+) [15]. HPV test can forecast cervical cancer risk many years in advance. Compared to the HPV test, the Pap test has a higher specificity of 97.9% but a lower sensitivity of 40.3% [16]. However, the Pap test and the HPV test cannot provide results in real time and cannot localize suspicious regions. While VIA can offer real time diagnosis and provide an alternative "see-and-treat" strategy for rural areas, it has a lower sensitivity of 61.7% and specificity of 58.5%, for detecting CIN2+, which has limited its extensive use [17]. Furthermore, visual inspection methods are variable between different investigators and require

biopsies to confirm diagnoses. The gold standard for diagnosis of cervical diseases is colposcopy-directed biopsy with histopathological confirmation. This technique has a sensitivity of 86.7% and a specificity of 90.4% [17]. Biopsies may offer the clearest diagnosis, but they are invasive and may cause complications such as bleeding, infections and discharge. Additionally, due to the invasive nature of biopsies, only a few superficial sites may be chosen for investigation. This increases the chance of missing lesions, leading to missed diagnoses. A recent study from China reported that colposcopy directed biopsy failed to detect up to 37% of high-grade lesions [18].

In 2010, 50.3% of the Chinese population were living in rural areas [19], where 90% of cervical cancer cases occur [20]. In these rural areas, there is a need for a cheap, efficient and easy-to-use approach for cervical cancer management. "See-and-treat" is a diagnosis and treatment strategy that has seen considerable interest for application in developing countries. In rural and developing regions, there can be an excedingly high patient dropout rate, so it is imperative to diagnose and treat patients in as few visits as possible. Currently the "see-and-treat" protocol recommends VIA for diagnosis, and cryotherapy or loop electrosurgical excision procedure (LEEP) for treament [14]. As VIA has low sensitivity and specificity, alternative strategies are needed to improve the performance of "see-and-treat" protocols.

Several non-invasive technologies are currently under investigation for use in cervical cancer screening procedures [21]. Cervical dysplasia and cancer often results in changes in nuclear morphology. Many novel non-invasive techniques focus on measuring nuclear size and eccentricity. For example, angle resolved low coherence interferometry can detect quantitative information about nuclear structure by measuring scattering properties of the cervical tissue [22, 23]. This technique can extract quantitative tissue information, but it is incapable of generating high-resolution images of tissue microarchitecture. High-resolution mircoendoscopy has also been used to measure the size and eccentricity of nuclei within cervical epithelial tissue [24]. Confocal microscopy can produce high-resolution images with molecularly specific information. Preliminary studies show that the nuclear/cytoplasmic ratio calculated from confocal images can be used to classify cervical cancer and dysplasia with high sensitivity [24]. Autofluorescence spectroscopy has also been used to detect cervical precancer and cancer by measuring chemical changes in tissue [25]. All of these techniques either lack depth resolving capabilities or have limited imaging

penetration depths, which could lead to missed diagnoses of deeper lesions.

Optical coherence tomogrophy (OCT) is an emerging medical diagnostic imaging modality that was first demonstrated in 1991 [26]. OCT uses near-infrared light interferometry to produce 3-D and cross-sectional images of internal tissue microstructures based on backscattering light. In most tissues, OCT can detect cellular and microarchitectural features with a resolution of ~3-20 µm and a penetration depth of about ~2 mm [27, 28]. Although imaging depths are not as deep as with ultrasound, the resolution of up to ~3 µm for OCT is as much as 50 to 100 times finer than standard clinical ultrasound and approaching that of histopathology. OCT, a standard of care for diagnosis of ophthalmic diseases such as diabetic retinopathy, has been applied to anterior segment imaging and ophthalmic intra-operative imaging [29-31]. In the cardiac field, OCT has also seen clinical adaptation for measurement of atherosclerosis plaques [32, 33]. Other fields, such as dermatology, endoscopy, dentistry, oncology [34], have been widely investigated. Optical coherence microscopy (OCM) is a branch of OCT with ultrahigh axial and lateral resolution [35, 36]. It can produce microscopic images with similar features to histology, opening up the possibility for it to be used as an optical biopsy tool. Recently OCM has shown promise in identifying cancer in breast, kidney, lymph nodes and thyroid tissues [37-41].

In 1999, the first *ex vivo* study using OCT on tissue of the female genital tract was performed [42]. In 2004, OCT was investigated *in vivo* to identify cervical precancerous and cancerous lesions [43]. Though those studies have shown that OCT has the potential to detect and differentiate grades of precursor and cancerous lesions [11, 18, 21, 27, 42, 44], images obtained in these studies have limited resolution (~10-20 µm), which limits the visualization of microarchitectural features. In this work, an ultrahigh-resolution OCM system providing cellular resolution (~1.8 µm) images was developed. Diagnostic features similar to histology were obtained from these high-resolution OCM images. The purpose of this study is to assess the diagnostic value of OCM for human cervical precancer and cancer screening and to identify characteristic features in OCM images, which will lay the foundation for future non-invasive optical evaluation of cervical tissue *in vivo*.

Methods

Ultrahigh-resolution OCM system

An ultrahigh-resolution, spectral-domain OCM system was developed at Lehigh University and moved to the Third Affiliated Hospital of Zhengzhou University for this project (**Figure 1A**). The OCM system is similar to what was published previously by our group [45, 46]. Briefly, a supercontinuum light source (NKT, SuperK EXTREME EXW-12) provides a broadband, near-infrared light centered at 800 nm with a bandwidth of ~250 nm. An axial resolution of ~1.8 µm and a transverse resolution of ~3.5 µm in tissue was achieved with a 10× Olympus objective. A 175° conical lens was used in the sample arm to generate an extended depth of focus of ~300 µm. A detection sensitivity of ~95 dB was achieved with ~10 mW of incident power on the sample at 20,000 A-scans/s image speed. Each 3-D OCM scan has 400 × 400 or 600 × 600 axial scans and the scan range was ~800 µm × 800 µm on the sample surface.

Study protocol and imaging procedures

The study was approved by the Institutional Review Board of the Third Affiliated Hospital of Zhengzhou University. 92 patients (mean age, 43 years; range, 20-85 years) at the Third Affiliated Hospital of Zhengzhou University with suspicious cytology findings (atypical squamous cells of undetermined significance (ASCUS)) or with positive HPV tests were recruited for the study. Among these patients, 51 were HPV positive, 32 were HPV negative, and 9 did not have a recorded HPV status. Fresh cervical specimens (n = 159) were collected via colposcopic biopsy (n = 79), conization (n = 26) or hysterectomy (n = 54). On average, ~1.6 samples were procured from each patient (for conization or hysterectomy specimens, up to 12 samples were obtained). Before imaging, cervical specimens were placed on a thin, wet sponge to keep the surface of the tissue flat and moist. OCM imaging was typically performed within 1 h of excision. On average, ~3.1 3-D OCM scans were acquired per specimen.

Gross photographs were taken of all the samples from each patient before OCM imaging. During scanning, cervical tissues were compressed from the sides by glass slides with the epithelium oriented towards the objective, and OCM imaging was performed from multiple locations at the surface of the cervix tissue. Each scan location was marked virtually on the gross picture using a red dot (**Figure 1B**). After imaging, the specimens were fixed in formalin and embedded in paraffin. Five micron-thick sections were cut along the cross-sectional OCM direction and stained with hematoxylin and eosin (H&E). The H&E slides were scanned by a Mixotic scanner. Histology sections were compared to the gross photograph by matching overall geometry and tissue landmarks. The recorded OCM locations from

the gross picture were projected to the corresponding histological section to the best of our ability (**Figure 1C**). An experienced pathologist reviewed each H&E histological section and provided diagnosis for each OCM imaging location (not for the whole slide) per the ACP/ASCCP 2012 lower genital squamous grading system. 3-D and cross-sectional OCM images were then matched to corresponding H&E histology from the same location as indicated in **Figure 1D-E**. This provided ground truth diagnosis for each 3-D OCM dataset used in our analysis. In total, 497 3-D OCM datasets were acquired from the 159 specimens. These datasets were classified into five groups: normal cervix (n = 197), ectropion (n = 79), LSIL (n = 28), HSIL (n = 55) and invasive lesions (n = 138). Invasive lesions included 134 squamous cell cancer datasets from 21 specimens and 4 adenocarcinoma image datasets from one specimen.

Image processing and analysis

OCM images were processed using a custom software and analyzed in Image J (http://rsbweb.nih.gov/ij/download.html, Bethesda, MD). OCM images were rescaled to have 1:1 aspect ratio in the transverse and axial direction in order to compare to corresponding histological slides. The H&E slides were scanned with a Mixotic scanner, and pictures were captured at 10x magnification. OCM images were matched with corresponding histology based on virtual locations marked on histological sections (**Figure 1C**). OCM imaging features useful for cervical disease diagnosis were identified and summarized through side-by-side comparison with histology.
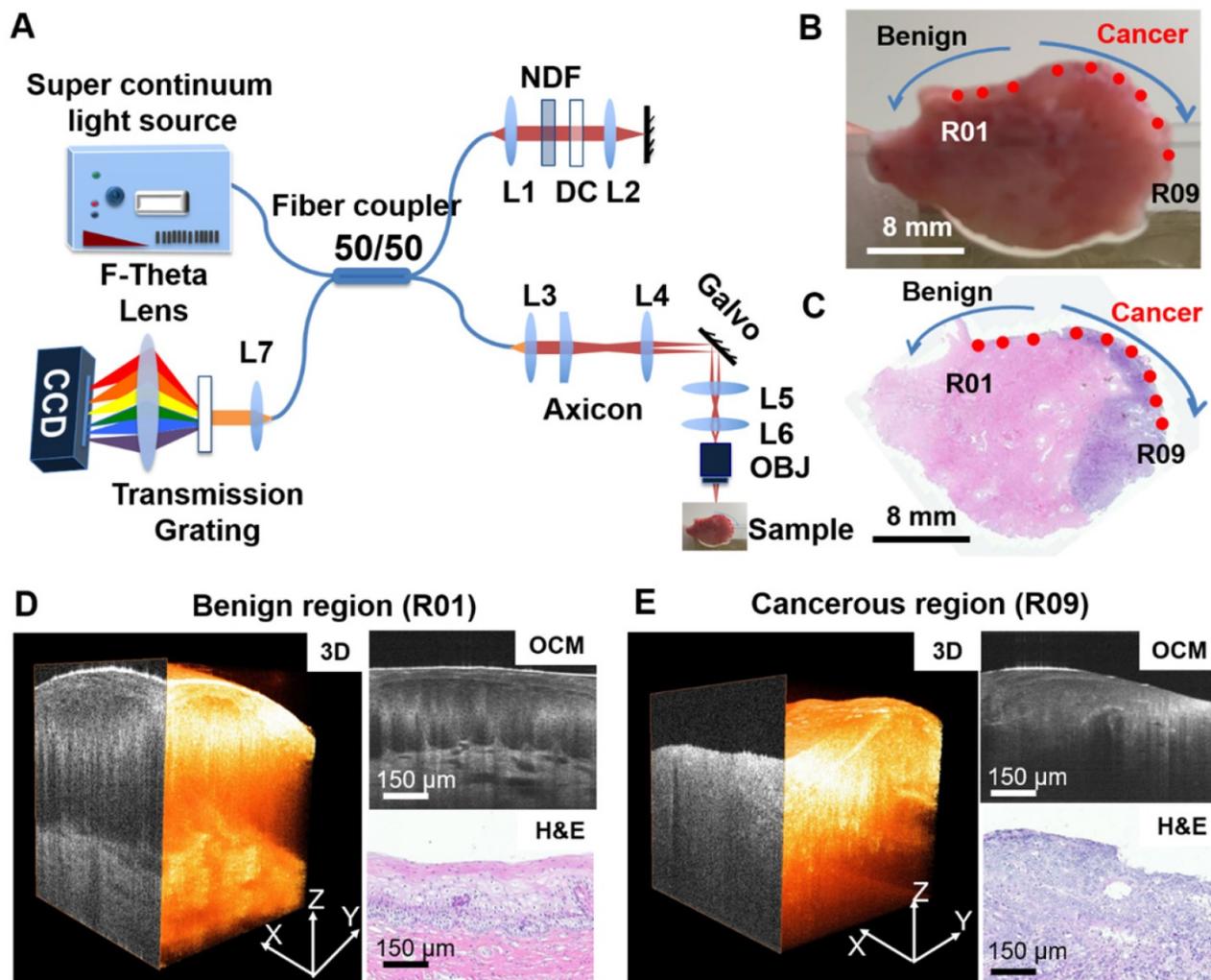

Figure 1. Summary of OCM imaging procedures. (A) Diagram of the ultrahigh-resolution OCM imaging system used in the project. **(B)** Cervical specimen gross image and corresponding histology. **(C)** OCM imaging locations were marked on the gross tissue picture using red dots (R01 to R09). The corresponding H&E slide from the same specimen was matched to the gross picture by tissue contour and structural landmarks. OCM imaging locations were projected to the H&E slide to obtain a ground truth diagnosis for each OCM dataset. **(D-E)** Representative 3-D OCM images, OCM cross sections, and corresponding H&E histology of a benign region (R01, (D)) and a cancerous region (R09, (E)) from locations shown in (B) and (C).

Blinded image classification and statistical analysis

Since there were no established diagnostic features for OCM imaging of human cervical tissue, we designed a three-step training and blinded-testing procedure to evaluate the diagnostic accuracy based on OCM images. Three investigators (investigator 1 is an experienced OCM researcher and investigators 2 and 3 are experienced pathologists) from three different institutes participated in the test. First of all, each investigator was provided a dataset including 100 3-D OCM images and corresponding H&E histological slides in digital form. After thoroughly reviewing all the training OCM images and corresponding histology to get familiarized with OCM imaging features, each investigator was presented a pre-testing dataset containing 100 separate 3-D OCM images. Each investigator was asked to make a diagnosis of the 3-D OCM images based on summarized image features and a diagnostic flow chart. After the pre-test, each investigator was given the correct diagnoses for misclassified samples. These datasets were thoroughly reviewed before each investigator performed the final blinded test. This pre-test and re-review process was important for investigators to get trained effectively in order to recognize diagnostic features from a new imaging technology within a short time. For the final test, 297 3-D OCM images were presented to each investigator to evaluate the diagnostic accuracy of OCM in differentiating high-risk from low-risk cervical tissues. For both the pre-test and final test, the three investigators were blinded to corresponding H&E slides and histological diagnosis. Only patient age and HPV status information was provided to the investigators. Multiple 3-D OCM images from the same specimen (if there were any) were only used in one of the training, pre-testing and final testing datasets. The ratios of sample number for each category used in all three dataset were maintained at about the same level.

Using histological diagnosis at each OCM imaging location as the ground truth, diagnostic accuracy, sensitivity, specificity, positive predictive value (PPV), and negative predictive value (NPV) were calculated for each investigator. Confusion matrixes for the three investigators and the 95% confidence interval (CI) for each statistical parameter was calculated. In addition, inter-observer agreement (κ value) between the three investigators were also calculated.

Results

OCM identifies diagnostic features shown in corresponding histological slides

Figure 2 shows OCM images and corresponding H&E histologic sections of low-risk cervical specimens, which includes normal cervix, mild inflammation, squamocolumnar junction, cervical ectropion and low-grade squamous intraepithelial lesions (LSIL). In normal specimens (**Figure 2A-B**), stratified squamous epithelium and stroma exhibit well-organized layered architecture in the cross-sectional OCM image. Stratified squamous cells form a mesh-like pattern. The interface between epithelium and stroma can be clearly observed, and fewer cellular details can be clearly identified close to the basal membrane layer (**Video S1**). For mild inflammation (**Figure 2C**), densely packed inflammatory cells cause the lower epithelium to exhibit hypo-scattering characteristics, while the superficial epithelium maintains its mesh-like structure. The interface between the epithelium and the stroma may be less clear than in the normal case. Inflammation cells infiltrating into the stroma and lower epithelial layer can be identified in the H&E section (**Figure 2D**).

Figure 2E-F depict OCM images and corresponding H&E histologic sections of the cervical squamocolumnar junction (SCJ). SCJ marks the boundary between the squamous-lined ectocervix and the columnar-lined endocervix. The transformation zone refers to the cervical area between old SCJ and new SCJ. Identification of the SCJ is crucial as 90% of precancerous lesions originate in the transformation zone. The SCJ (arrow) can be easily identified in the OCM image (**Figure 2E**). In the region around the SCJ, glands with mucous secretions can be observed in **Figure 2E** and **Video S2**, which have good correspondence with the H&E section (**Figure 2F**). In **Figure 2E** the monolayer of columnar cells and junction cells has been replaced by several layers of squamous metaplasia cells (SM). Additionally, mucus accumulation, which results in the formation of Nabothian cysts (NC), can be observed. These are likely caused by the blockage of glandular ducts or periglandular fibrosis.

Figures 2G-L exhibit OCM images and corresponding H&E histologic sections of ectropion at the SCJ. For ectropion tissue, stratified squamous epithelial cells are replaced by single layers of columnar mucus-producing epithelium cells (**Figure 2H, J**). The epithelium loses its layered architecture and forms regular papillary or glandular structures with hyper-scattering boundaries that can be clearly visualized in OCM images (**Figure 2G, I** and **Video S3**). When chronic cervical inflammation begins to

heal, the single layer of columnar cells is replaced by several layers of squamous metaplasia cells, which are visible (arrow) in the H&E section (**Figure 2L**). In the OCM image (**Figure 2K**), this multi-layer of squamous metaplasia cells takes on a hypo-scattering appearance.

Typical OCM features and corresponding H&E histologic sections of LSIL are demonstrated in **Figures 2M-R**. Condyloma or CIN1 are the most common types of LSIL. Condyloma is a state of low-risk HPV infection (subtypes 6 and 11). Koilocytic cells are clearly visible in **Figure 2M-N** and **Video S4**. Their enlarged nuclei and perinuclear halos are representative features of low-risk HPV infections. In a typical OCM image of CIN1 (**Figure 2O**), unstructured hypo-scattering regions (brace) in the lower third of the epithelium can be identified. Hypo-scattering squamous metaplasia (SM) coexisting with CIN1 can be visualized in **Figure 2Q**; they share similar hypo-scattering features in the OCM image. **Video S5** shows that the shape of the gland shown in **Figure 2Q** changes drastically through different B-scan frames, indicating that more structural information can be obtained with the 3-D OCM images than with H&E sections.

Figure 3 shows OCM features and corresponding H&E histologic sections of high-risk cervical specimens, including HSIL and invasive lesions. For CIN2 specimens, normal epithelial architecture is lost for more than one-third of the epithelium (**Figure 3A-B**), but the interface between squamous epithelium and stroma is still clearly delineated by the basal membrane in the OCM image (**Video S6**). For CIN3, OCM shows unstructured hyper-scattering features (**Figure 3C, E**), matching well with hyperplasia observed throughout the whole epithelium in H&E sections (**Figure 3D, F**). The interface between epithelium and stroma may be visible (**Figure 3A, E**), albeit less clearly than the normal tissue interface (**Figure 3C**). We observed that the epithelium and stroma are hyper-scattering, and epithelial brightness typically increases with the degree of dysplasia, but decays more quickly with depth than for normal tissue (**Figure 3C**). These findings were consistent with previous reports [47].

Figures 3G-L show OCM features and corresponding H&E histologic sections of invasive lesions. Nests, clusters or sheets of squamous cell tumors (T) can be identified in **Figure 3G, I, K**, respectively. We observed invasive lesions with unstructured, homogeneous hyper-scattering features in **Figure 3G** (see **Video S7**). However, we also observed heterogeneous characteristics (**Figure 3I, K**) and hyper-scattering desmoplastic reaction regions (arrow) infiltrated with tumor cells (**Video S8**). **Figure 3K** is an example of adenocarcinoma in an OCM image, in which sheets of tumor cells infiltrate into surrounding regions, exhibiting heterogeneous features. A solitary nodule structure can also be easily visualized.
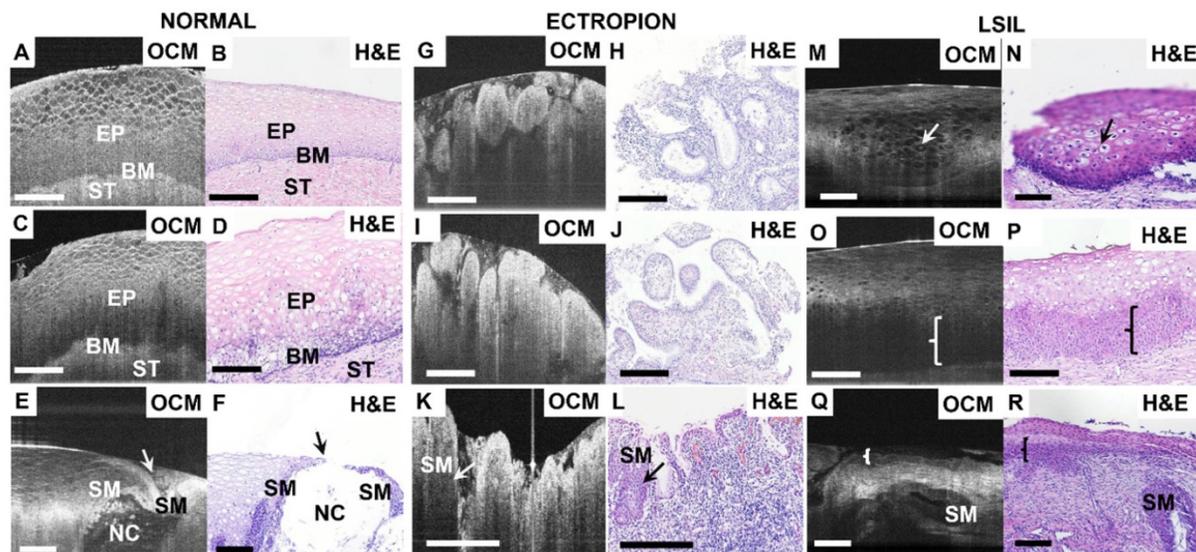

Figure 2. Typical OCM images and corresponding H&E histologic sections of low-risk cervical tissues. OCM images of normal ((**A**), 3D scan shown in **Video S1**) and mild inflammation (**C**) cervical specimens and corresponding histology (**B, D**). The interface between the epithelium (EP) and stroma (ST), e.g., the basal membrane (BM), can be clearly visualized. OCM image ((**E**), 3D scan shown in **Video S2**) and corresponding H&E histologic sections (**F**) of the squamocolumnar junction (SCJ). In (E) and (F), a Nabothian cyst (NC) and multi-layer squamous metaplasia (SM) cells were observed. OCM images (**G, I, K**) and H&E histologic sections (**H, J, L**) of cervical ectropion. Regular papillary structure with sharp hyper-scattering boundaries are visible in OCM images (G, I) which is consistent with ectropion at the transformation zone and single layered glandular structures (H, J). In (K) and (L), columnar cells and multiple layers of SM cells (arrows in (K-L)) were seen at the transition zone with underlying intense chronic inflammation, which have hypo-scattering features in the OCM image. 3D OCM scan of (G) is shown in **Video S3**. OCM images (**M, O, Q**) and corresponding H&E histologic sections (**N, P, R**) of low-grade squamous intraepithelial lesions (LSIL). (M) and (N) exhibited representative features of Condyloma (see **Video S4**). Koilocytotic cells were clearly visible in OCM image and H&E section. (O) and (Q) demonstrate characteristic features of CIN1 in OCM images. The cells in the lower third of the epithelium show hypo-scattering features (brace) in the OCM image (O). Glands with SM and CIN1 (brace) share similar hypo-scattering characteristics ((Q), 3D scan shown in **Video S5**). Scale bars: 150 μm.
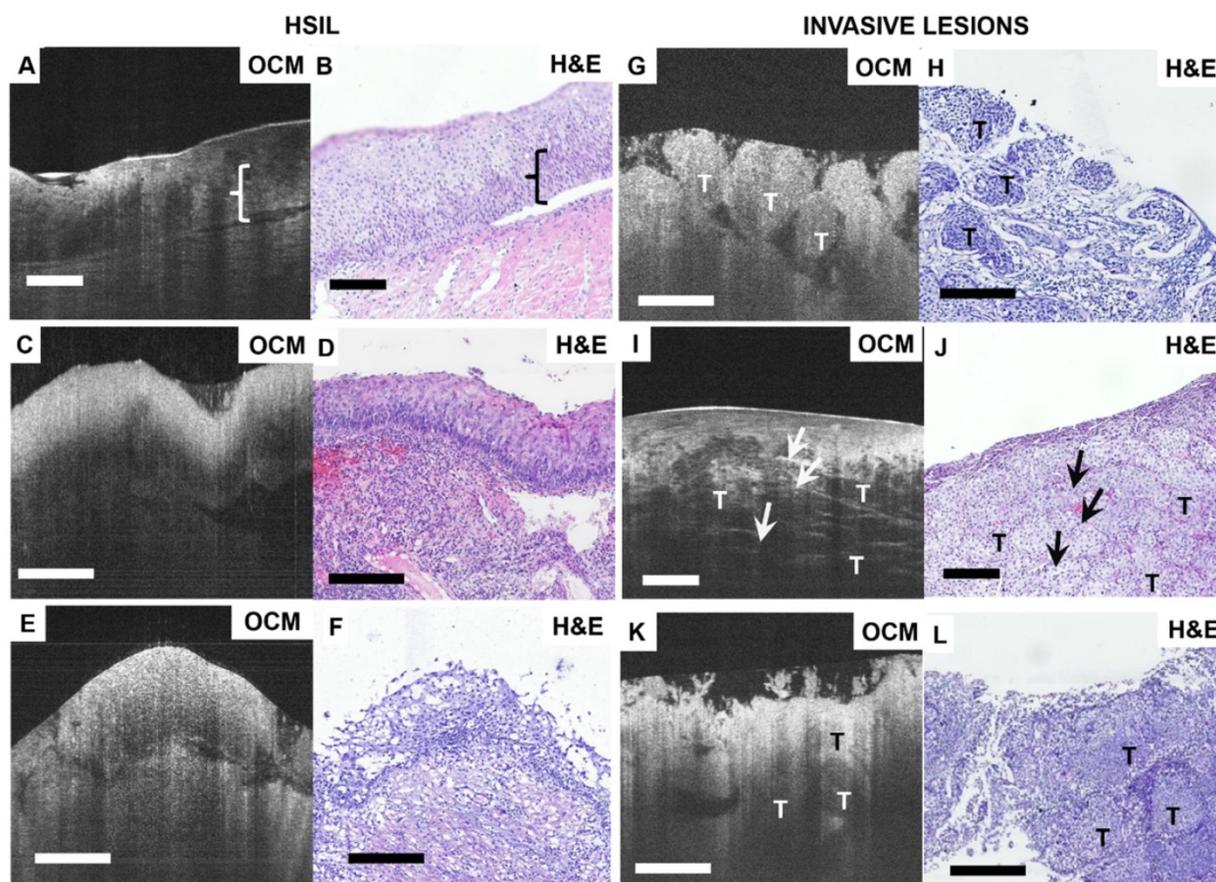
Figure 3. Typical OCM and corresponding histology images of high-risk cervical tissues. OCM images **(A, C, E)** and corresponding H&E histologic sections **(B, D, F)** of high-grade squamous intraepithelial lesions (HSIL). The interface between the epithelium layer and stroma still can be found (A, E) but may be less clear (C). 3D OCM scan of (A) is shown in **Video S6**. OCM images **(G, I, K)** and corresponding H&E histologic sections **(H, J, L)** of invasive lesions. Nests ((G), 3D scan shown in **Video S7**), clusters ((I), 3D scan shown in **Video S8**) or sheets (K) of homogeneous (G) or heterogeneous regions (I, K) can be identified in the OCM images. (I) exhibits hyper-scattering desmoplastic reaction (arrows) with fibrous stroma tissue visible. OCM images of adenocarcinoma (K) share heterogeneous characteristics with squamous cancer images (G). T: tumor. Scale bars: 150 μm.

Figure 4 compares 3-D OCM image features of normal cervix, ectropion and invasive lesions. A 3-D rendering of normal cervix (**Figure 4A**) shows structured mesh-like epithelium with a smooth surface. **Figure 4B** shows an *en face* slice of the 3-D dataset, as indicated in **Figure 4A**. Cellular membranes and cell nuclei display hyper-scattering features, while cytoplasm has hypo-scattering characteristics, which contribute to the mesh-like structure of the epithelium. Individual cell nuclei (arrows) can be clearly identified from the *en face* images (**Figure 4B-C**, arrows). A 3-D image of cervical ectropion (**Figure 4D**) has much less organized features than normal cervical tissue. Glandular structure with a sharp boundary (arrows) can be clearly identified from the *en face* OCM image of ectropion (**Figure E-F**). An invasive lesion shown in **Figure 4G** has no glandular structures; only unstructured tumor nests were observed (**Figure 4H-I**). A summary of optical features for various cervical lesions is presented in **Table 1**.

Blinded image classification and statistical analysis

Blinded image classification was performed in three steps according to the protocol described in Methods. Three investigators were asked to make their diagnosis of each 3-D OCM dataset based on the optical features shown in **Table 1** and the flow chart shown in **Figure 5A**. Normal, ectropion and LSIL specimens were classified as low-risk, while HSIL and invasive lesions were classified as high-risk. Confusion matrixes detailing the blinded diagnosis results from the three investigators are shown in **Figure 5B**. **Table 2** summarizes the statistical results. Overall diagnostic accuracy for the three investigators was 89%, 83% and 85%, respectively. Though the three investigators obtained a range of sensitivities from 65% to 92%, they all achieved high specificity (86% to 94%). On average, a sensitivity of 80% and a specificity of 89% was achieved, with a positive predictive value (PPV) of 83% and a negative predictive value (NPV) of 88%. A κ value of 0.627

indicates substantial agreement among the three observers. It is noted that investigator 2 (a pathologist) has the lowest sensitivity (65%), NPV (81%) and overall accuracy (83%), but the highest specificity (94%) and PPV (87%). This may be attributed partially to insufficient training with OCM images.
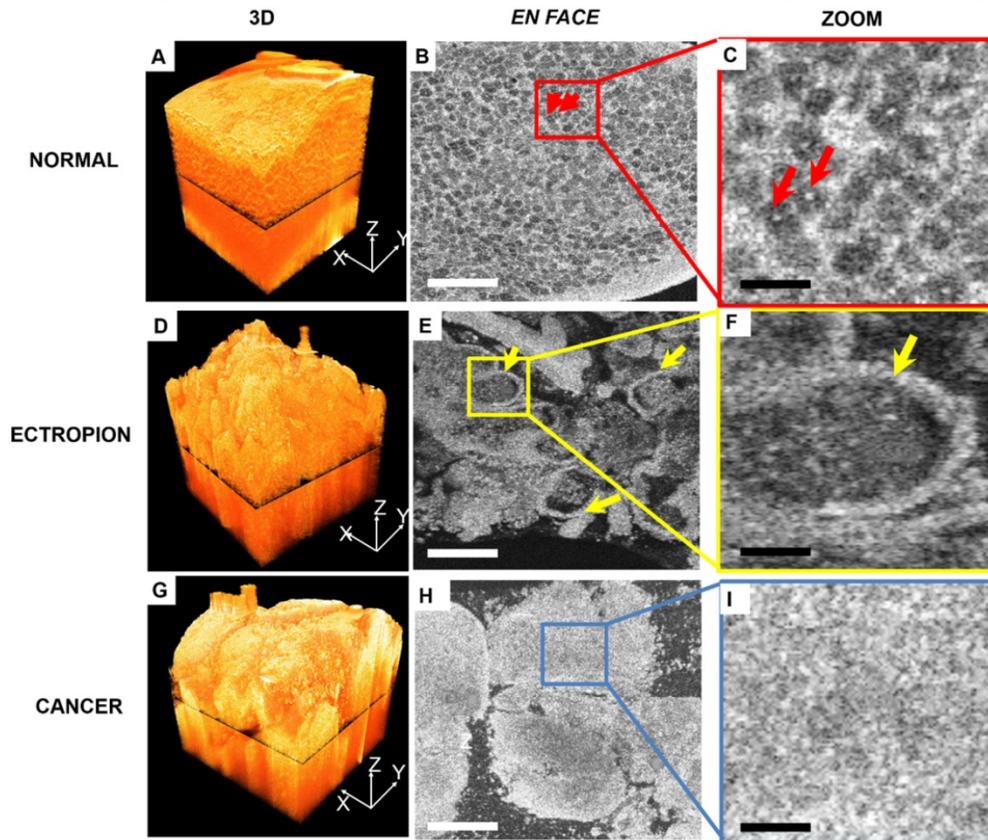

Figure 4. 3-D and *en-face* OCM images of normal cervical epithelium, ectropion and invasive lesions. (A) 3-D OCM images of normal cervix show uniform structure throughout the 3-D volume. In the *en face* OCM image of normal epithelium, cellular membranes and cell nuclei display hyper-scattering features, while cytoplasm has hypo-scattering characteristics, which contribute to the mesh-like structure of epithelium. Individual cell nuclei (arrows) can be clearly identified from the images ((**B-C**), 5x magnification). **(D)** 3-D image of cervical ectropion has much less organized features than normal cervical tissue. In the *en face* OCM image of ectropion **(E-F)**, glandular structure with sharp boundary (arrows) can be clearly identified. Invasive lesions shown in the 3-D image **(G)**, and *en face* images **(H-I)** have no glandular structures, but only unstructured tumor nests were observed. Scale bars: 150 µm in (B, E, H) and 30 µm in (C, F, I).

Table 1. Optical features of different cervical lesions on OCM.

Category	Optical features
Normal	Epithelial squamous cells show stratified mesh-like architecture, the epithelium and stroma are clearly separated by the basal membrane and form a layered architecture, and a sharp interface is discernible.
Ectropion	Lose normal stratified structure and present regular papillary or glandular structures with hyper-scattering sharp boundaries.
LSIL	Characteristic koilocytotic cells (enlarged nuclei with cytoplasmic halos) are identified or the lower third of the epithelium loses regular architecture and shows hypo-scattering features.
HSIL	More than one third of the epithelium loses regular architecture and the boundary between the epithelium may be clear or less clear.
Invasive lesions	Lose layered structure between epithelium and stroma, and clusters, sheets or nests of homogeneous or heterogeneous structures with or without desmoplastic reaction regions can be found.

OCM: optical coherence microscopy; LSIL: low-grade squamous intraepithelial lesion; HSIL: high-grade squamous intraepithelial lesion

Table 2. Results from blinded diagnosis of 3-D OCM images from three independent investigators.

	Classification Results (95% CI)			
Investigator	1	2	3	Average (95% CI)
Accuracy	89%	83%	85%	85%
Sensitivity	92% (86% - 96%)	65% (56% - 74%)	82% (74% - 88%)	80% (72% - 86%)
Specificity	87% (81% - 91%)	94% (89% - 97%)	86% (80% - 91%)	89% (84% - 93%)
PPV	82% (75% - 87%)	87% (79% - 93%)	79% (72% - 85%)	83% (76% - 88%)
NPV	95% (90% - 97%)	81% (77% - 85%)	88% (84% - 92%)	88% (84% - 91%)
κ value	0.627			

LSIL: low-grade squamous intraepithelial lesion; PPV: positive predictive value; NPV: negative predictive value; CI: confidence interval.
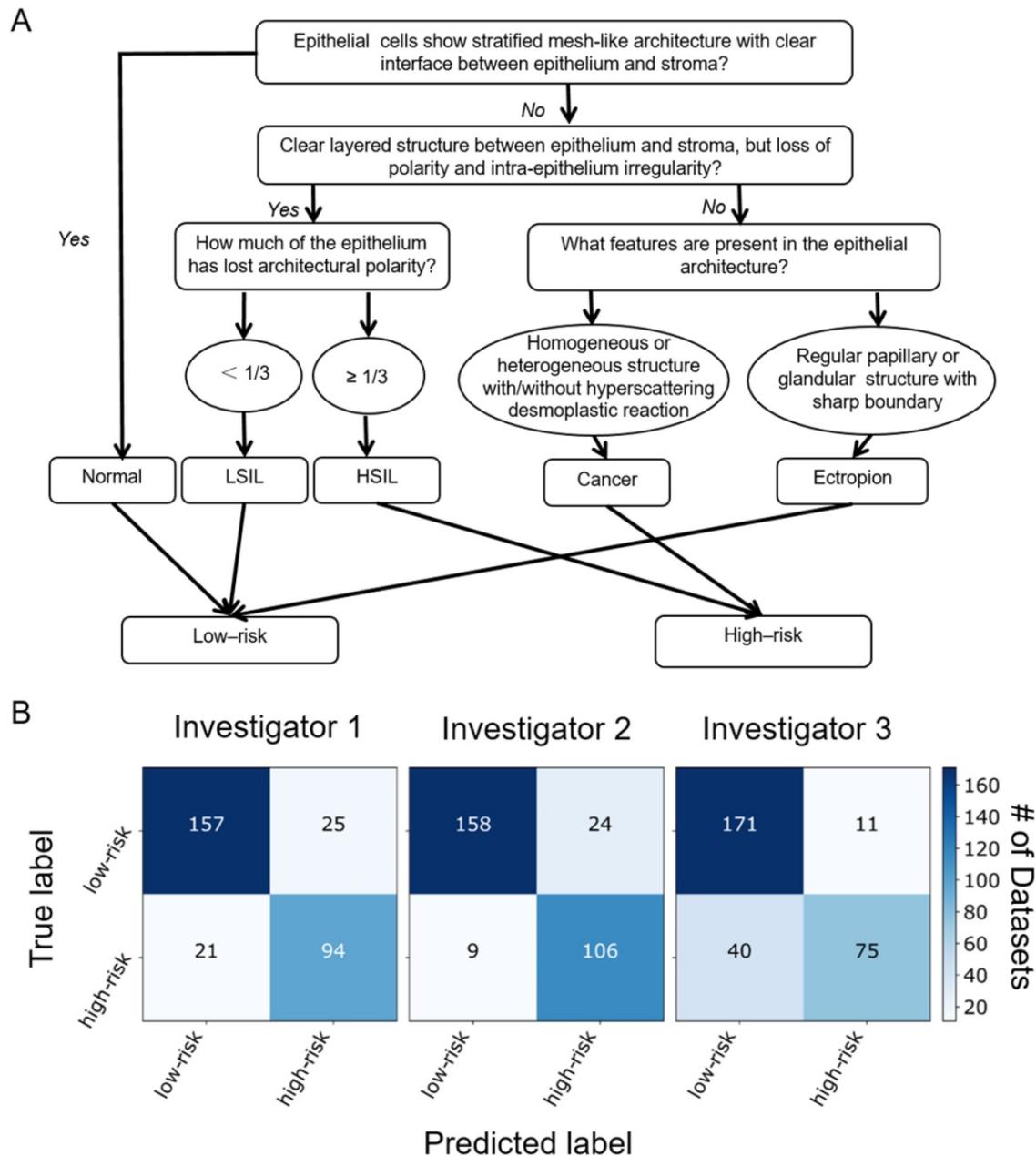
Figure 5. (A) Flow chart for OCM classification of cervical lesions. OCM diagnoses were based on the features of epithelial cell morphology, and epithelial and stromal architecture. Cellular changes typical of HPV infections with characteristic enlarged nuclei and perinuclear halos were not included in the flowchart. **(B)** Blinded diagnosis results for low-risk vs. high-risk classification from three investigators.

Discussion and conclusions

Ultrahigh-resolution OCM shows detailed characteristic features for each of the stages of human cervical lesions, which is a significant improvement upon past studies. Due to low resolution (~10-20 μm), previous studies relied on bulk features such as thickness of the epithelium, brightness contrast between the epithelium and stroma, status of the basement membrane, and brightness intensity profile of the epithelium for diagnosis [18, 27]. These features, while useful, may not be consistent with diagnostic features shown in gold standard H&E

histological slides. Even with realtively low resolution, sensitivity and specificity for detecting precancerous and cancerous lesions with OCT have been reported to be 95% and 46%, respectively [48]. With a threshold at CIN 2, the same group reported a sensitivity and specificity of 80%-86% and 60-64%, respectively [27]. By adding OCT to colposcopy, Liu *et al.* showed that the specificity for detecting CIN 2+ increased from 83% to 93%, but the sensitivity decreased [18]. Guided by a surgical microscope, the sensitivity and specificity for detecting HSIL with OCT have been reported as high as 88% and 69%,

respectively [49]. With an axial resolution of ~1.8 μm, our OCM system clearly revealed microstructures of squamous epithelium, columnar epithelium, SCJ, basement membrane, stroma, glands and invasive tumors, which matched well with corresponding histological slides. The ability to resolve cellular features with OCM enabled us to make low-risk vs. high-risk diagnosis of human cervical lesions with high accuracy (e.g., a sensitivity of 80%, a specificity of 89%, and an overall accuracy of 85%).

We showed that invasive lesions can be manifested as unstructured, homogeneous hyper-scattering features, which is consistent with a previous report [43]. We also demonstrated that invasive lesions may also have heterogeneous characteristics, especially for hyper-scattering desmoplastic reaction regions infiltrated with tumor cells. To our knowledge, these heterogeneous features have only been demonstrated by Pitris *et al.* [42] These heterogeneous features are likely caused by the pleomorphism of tumor cells (increased nuclear size, increased nuclear-to-cytoplasmic ratio, hyperchromasia, and binuclear or multinuclear cells). Hyper-scattering desmoplastic reaction, a valuable feature for identifying invasive cancer tissue in H&E sections, as well as the koilocytotic cells infected with HPV, were first observed in our ultrahigh-resolution OCM images.

As a developing technique, OCM still has some limitations. In our blinded diagnosis study, ~20% of misclassification occurs between ectropion and invasive lesions. Both disease states have similar irregular features in 2-D OCM images, which can be difficult to differentiate, even for well-trained observers. OCM provides 3-D images, which can be viewed from different orientations. As shown in **Figure 4**, ectropion and invasive lesions show very different image features in the *en face* plane obtained from the 3-D OCM stack, demonstrating the benefits of 3-D imaging. We have not identified consistent OCM features that would allow us to differentiate invasive cancer from high-grade precancerous disease and immature squamous metaplasia. Due to this limitation, cancer diagnoses cannot be made using OCM images alone at the current stage. There have been studies to explore objective methods for differentiation; these methods include measuring backscattering intensity or brightness [44, 47, 50]. Parameters and methods that can be used for discriminating grades of CIN lesions from invasive disease need to be explored further in future studies.

OCM images from this *ex vivo* study match well with histology. However, additional complications may be encountered in an *in vivo* environment. These potential complications include motion artifacts, bleeding, abnormal vaginal secretion, irregular cervical surface, etc. These challenges need to be further investigated through *in vivo* clinical studies, and addressed properly before the technology can be widely adopted in the clinic in the future.

One of the key advantages of OCM is that it can provide real-time, *in vivo* imaging without removing or processing tissue. OCM can be integrated into small diameter probes or catheters, endoscopes, laparoscopes, and needles for early cancer detection [51, 52], which enable OCM to be widely used in the clinic. We are in the process of developing and validating OCM imaging probes that can be used in human patients *in vivo*. In addition, since OCM is a new imaging technology, it may be challenging for pathologists and gynecologists to learn to make diagnoses based on OCM images. The learning curve is expected to be steep and the diagnostic accuracy of each individual may be heavily dependent on training experience. It is therefore critical to develop an objective method to make real-time diagnosis. With the advent of deep learning, neural network classification models, and high-speed graphics processing unit (GPU) computing, it has become possible to develop algorithms that automatically diagnose disease and segment diseased regions from OCM images. This will significantly improve diagnostic accuracy and facilitate the adoption and clinical translation of OCM technology. We envision a diagnostic system where *in vivo* OCM imaging probes can be used in conjunction with a computer-aided diagnosis program to rapidly map suspicious disease regions on the cervix. These maps can be used to accurately screen at-risk populations.

OCM images can be used to provide more precise information of the content and extent of suspicious sites, which would be useful for guiding colposcopy-directed biopsies. As a complement to VIA or colposcopy, ultrahigh-resolution OCM could guide biopsies to improve the accuracy of biopsy localization, and at the same time reduce or minimize the number of unneeded biopsies. The reduced number of necessary biopsies would reduce strain on existing health care systems. In developing countries, such as in Central Asia and some countries of Central and Eastern Europe, where infrastructure and resources are limited, OCM can provide a complementary diagnostic approach for "see-and-treat" strategies. Additionally, OCM provides higher sensitivity (80% vs. 61.7%) and specificity (89% vs. 58.5%) than VIA for detecting CIN2+ lesions. Combining OCM and VIA is expected to achieve even more accurate guidance for targeted biopsies, reducing the invasiveness and increasing the efficacy of the procedure.

In summary, through careful comparison of 497 3-D OCM images and corresponding H&E histology from 159 *ex vivo* cervical specimens from 92 human patients, we identified diagnostic OCM features of different types of human cervical lesions, ranging from normal cervix, ectropion, LSIL, HSIL, to invasive cancer. Three independent investigators, blinded from histological diagnosis, achieved a sensitivity of 80% (95% CI, 72% - 86%), a specificity of 89% (95% CI, 84% - 93%) and overall accuracy of 85% to differentiate low-risk and high-risk cervical lesions. With further refinement, ultrahigh-resolution OCM has the potential to become a complementary tool for cervical cancer screening, and may play an important role in the "see-and-treat" strategy for the management of cervical cancer.

Abbreviations

3-D: 3-dimensional; ASCUS: atypical squamous cells of undetermined significance; CI: confidence interval; CIN: cervical intraepithelial neoplasia; GPU: graphics processing unit; H&E: hematoxylin and eosin; HPV: human papillomavirus; HSIL: high-grade squamous intraepithelial lesions; LEEP: loop electrosurgical excision procedure; LSIL: low-grade squamous intraepithelial lesions; NPV: negative predictive value; NC: nabothian cysts; OCM: optical coherence microscopy; OCT: optical coherence tomography; Pap test: Papanicolaou test; PPV: positive predictive value; SCJ: squamocolumnar junction; SM: squamous metaplasia; VIA: visual inspection of cervix with acetic acid; WHO: world health organization.

Supplementary Material

Video S1. http://www.thno.org/v08p3099s1.mov
Video S2. http://www.thno.org/v08p3099s2.mov
Video S3. http://www.thno.org/v08p3099s3.mov
Video S4. http://www.thno.org/v08p3099s4.mov
Video S5. http://www.thno.org/v08p3099s5.mov
Video S6. http://www.thno.org/v08p3099s6.mov
Video S7. http://www.thno.org/v08p3099s7.mov
Video S8. http://www.thno.org/v08p3099s8.mov
Captions for supplementary videos.
http://www.thno.org/v08p3099s9.pdf

Acknowledgments

Contributions

C.Z. built the imaging system and designed the experiments. X.X.Z., X.A.Z., X.F.W., L.L.Z. and Z.Z. collected the specimens and acquired the raw data. C.Y.L., T.X., X.F.W., Y.N. and Y.T.M. processed the images and analyzed the data. C.Z., X.X.Z. and Y.H.W. performed the blinded image classification test. C.Y.L., J.J., X.X.Z. and C.Z. wrote the manuscript. All other authors reviewed and edited the manuscript. C.Z. oversaw the entire project.

Competing Interests

C.Z. is an inventor of related patents owned by Lehigh University and declares financial interests in SDM Innovations, Inc., which did not support the current project. Other authors declare no competing financial interests.

References

1. Gaffney D, Small B, Kitchener H, Young Ryu S, Viswanathan A, Trimble T, et al. Cervix cancer research network (CCRN): improving access to cervix cancer trials on a global scale. Int J Gynecol Cancer. 2016; 26: 1690-3.
2. Torre LA, Siegel RL, Ward EM, Jemal A. Global cancer incidence and mortality rates and trends--an update. Cancer Epidemiol Biomarkers Prev. 2016; 25: 16-27.
3. Globocan 2012: estimated cancer incidence, mortality and prevalence worldwide in 2012. International Agency for Research on Cancer; 2012.
4. American Cancer Society, Cancer facts & figures 2016. Atlanta: American Cancer Society; 2016.
5. Chokunonga E, Borok MZ, Chirenje ZM, Nyakabau AM, Parkin DM. Trends in the incidence of cancer in the black population of Harare, Zimbabwe 1991-2010. Int J Cancer. 2013; 133: 721-9.
6. Bray F, Lortet-Tieulent J, Znaor A, Brotons M, Poljak M, Arbyn M. Patterns and trends in human papillomavirus-related diseases in Central and Eastern Europe and Central Asia. Vaccine. 2013; 31 Suppl 7: H32-45.
7. Chen W, Zheng R, Baade PD, Zhang S, Zeng H, Bray F, et al. Cancer statistics in China, 2015. CA Cancer J Clin. 2016; 66: 115-32.
8. Wang B, He M, Chao A, Engelgau MM, Saraiya M, Wang L, et al. Cervical cancer screening among adult women in China, 2010. Oncologist. 2015; 20: 627-34.
9. Pierce Campbell CM, Menezes LJ, Paskett ED, Giuliano AR. Prevention of invasive cervical cancer in the United States: past, present, and future. Cancer Epidemiol Biomarkers Prev. 2012; 21: 1402-8.
10. Reeler A, Qiao Y, Dare L, Li J, Zhang AL, Saba J. Women's cancers in developing countries: from research to an integrated health systems approach. Asian Pac J Cancer Prev. 2009; 10: 519-26.
11. Pandey K, Bhagoliwal A, Jain S. Optical imaging: future tool in detection of pre-cancerous and cancerous lesions of cervix and its comparison to colposcopy. J Obstet Gynecol India. 2015; 65: 176-80.
12. Schiffman M, Castle PE, Jeronimo J, Rodriguez AC, Wacholder S. Human papillomavirus and cervical cancer. Lancet. 2007; 370: 890-907.
13. Committee on Practice Bulletins - Gynecology. Practice bulletin No. 168: cervical cancer screening and prevention. Obstet Gynaecol. 2016; 128: e111-30.
14. World Health Organization. WHO guidelines for screening and treatment of precancerous lesions for cervical cancer prevention. Geneva: World Health Organization; 2013.
15. Arbyn M, Sasieni P, Meijer CJ, Clavel C, Koliopoulos G, Dillner J. Chapter 9: Clinical applications of HPV testing: a summary of meta-analyses. Vaccine. 2006; 24 Suppl 3: S3/78-89.

16. Wright TC, Stoler MH, Behrens CM, Sharma A, Zhang G, Wright TL. Primary cervical cancer screening with human papillomavirus: end of study results from the ATHENA study using HPV as the first-line screening test. Gynecol Oncol. 2015; 136: 189-97.

17. Singh V, Parashari A, Gupta S, Sodhani P, Sehgal A. Performance of a low cost magnifying device, Magnivisualizer, versus colposcope for detection of pre-cancer and cancerous lesions of uterine cervix. J Gynecol Oncol. 2014; 25: 282-6.

18. Liu Z, Belinson SE, Li J, Yang B, Wulan N, Tresser NJ, et al. Diagnostic efficacy of real-time optical coherence tomography in the management of preinvasive and invasive neoplasia of the uterine cervix. Int J Gynecol Cancer. 2010; 20: 283-7.

19. Communiqué of the National Bureau of Statistics of People's Republic of China on Major Figures of the 2010 Population Census(NO.1). National Bureau of Statistics of the People's Republic of China; 2011.

20. Wen C. China's plans to curb cervical cancer. Lancet Oncol. 2005; 6: 139-41.

21. Novikova T. Optical techniques for cervical neoplasia detection. Beilstein J Nanotechnol. 2017; 8: 1844-62.

22. Wax A, Yang CH, Backman V, Badizadegan K, Boone CW, Dasari RR, et al. Cellular organization and substructure measured using angle-resolved low-coherence interferometry. Biophys J. 2002; 82: 2256-64.

23. Ho D, Drake TK, Smith-McCune KK, Darragh TM, Hwang LY, Wax A. Feasibility of clinical detection of cervical dysplasia using angle-resolved low coherence interferometry measurements of depth-resolved nuclear morphology. Int J Cancer. 2017; 140: 1447-56.

24. Quinn MK, Bubi TC, Pierce MC, Kayembe MK, Ramogola-Masire D, Richards-Kortum R. High-resolution microendoscopy for the detection of cervical neoplasia in low-resource settings. PLoS One. 2012; 7: e44924.

25. Drezek R, Brookner C, Pavlova I, Boiko I, Malpica A, Lotan R, et al. Autofluorescence microscopy of fresh cervical-tissue sections reveals alterations in tissue biochemistry with dysplasia. Photochem Photobiol. 2001; 73: 636-41.

26. Huang D, Swanson EA, Lin CP, Schuman JS, Stinson WG, Chang W, et al. Optical coherence tomography. Science. 1991; 254: 1178-81.

27. Gallwas JK, Turk L, Stepp H, Mueller S, Ochsenkuehn R, Friese K, et al. Optical coherence tomography for the diagnosis of cervical intraepithelial neoplasia. Lasers Surg Med. 2011; 43: 206-12.

28. Assayag O, Antoine M, Sigal-Zafrani B, Riben M, Harms F, Burcheri A, et al. Large field, high resolution full-field optical coherence tomography: a pre-clinical study of human breast tissue and cancer assessment. Technol Cancer Res Treat. 2014; 13: 455-68.

29. Regatieri CV, Branchini L, Carmody J, Fujimoto JG, Duker JS. Choroidal thickness in patients with diabetic retinopathy analyzed by spectral-domain optical coherence tomography. Retina. 2012; 32: 563-8.

30. Ramos JL, Li Y, Huang D. Clinical and research applications of anterior segment optical coherence tomography - a review. Clin Exp Ophthalmol. 2009; 37: 81-9.

31. Ray R, Baranano DE, Fortun JA, Schwent BJ, Cribbs BE, Bergstrom CS, et al. Intraoperative microscope-mounted spectral domain optical coherence tomography for evaluation of retinal anatomy during macular surgery. Ophthalmol. 2011; 118: 2212-7.

32. De Rosa R, Vasa-Nicotera M, Leistner DM, Reis SM, Thome CE, Boeckel JN, et al. Coronary atherosclerotic plaque characteristics and cardiovascular risk factors - insights from an optical coherence tomography study. Circ J. 2017; 81:1165-73.

33. Lee T, Murai T, Isobe M, Kakuta T. Impact of coronary plaque morphology assessed by optical coherence tomography on cardiac troponin elevation in patients with non-ST segment elevation acute coronary syndrome. Catheter Cardiovasc Interv. 2017; 90: 905-914.

34. Fujimoto J, Swanson E. The development, commercialization, and impact of optical coherence tomography. Invest Ophthalmol Vis Sci. 2016; 57: Oct1-Oct13.

35. Izatt JA, Hee MR, Owen GM, Swanson EA, Fujimoto JG. Optical coherence microscopy in scattering media. Opt Lett. 1994; 19: 590-2.

36. Aguirre A, Zhou C, Lee H, Ahsen O, Fujimoto J. Optical coherence microscopy. In: Drexler W, Fujimoto JG, editors. Optical Coherence Tomography: Springer International Publishing; 2015. p. 865-911.

37. Nolan RM, Adie SG, Marjanovic M, Chaney EJ, South FA, Monroy GL, et al. Intraoperative optical coherence tomography for assessing human lymph nodes for metastatic cancer. BMC cancer. 2016; 16: 144.

38. Erickson-Bhatt SJ, Nolan R, Shemonski ND, Adie SG, Putney J, Darga D, et al. In vivo intra-operative breast tumor margin detection using a portable OCT system with a handheld surgical imaging probe. Proc. SPIE. 2014; 8935: 89351C.

39. Zhou C, Wang Y, Aguirre AD, Tsai TH, Cohen DW, Connolly JL, et al. Ex vivo imaging of human thyroid pathology using integrated optical coherence tomography and optical coherence microscopy. J Biomed Opt. 2010; 15: 016001.

40. Zhou C, Cohen DW, Wang YH, Lee HC, Mondelblatt AE, Tsai TH, et al. Integrated optical coherence tomography and microscopy for ex vivo multiscale evaluation of human breast tissues. Cancer Res. 2010; 70: 10071-9.

41. Lee HC, Zhou C, Cohen DW, Mondelblatt AE, Wang YH, Aguirre AD, et al. Integrated optical coherence tomography and optical coherence microscopy imaging of ex vivo human renal tissues. J Urol. 2012; 187: 691-9.

42. Pitris C, Goodman A, Boppart SA, Libus JJ, Fujimoto JG, Brezinski ME. High-resolution imaging of gynecologic neoplasms using optical coherence tomography. Obstet Gynaecol. 1999; 93: 135-9.

43. Escobar PF, Belinson JL, White A, Shakhova NM, Feldchtein FI, Kareta MV, et al. Diagnostic efficacy of optical coherence tomography in the management of preinvasive and invasive cancer of uterine cervix and vulva. Int J Gynecol Cancer. 2004; 14: 470-4.

44. Gallwas J, Mortensen U, Gaschler R, Stepp H, Ditsch N, Friese K, et al. Diagnostic efficacy of backscattering intensity measurements in optical coherence tomography of cervical intraepithelial dysplasia. Lasers Surg Med. 2012; 44: 11-9.

45. Li F, Xu T, Nguyen DHT, Huang XL, Chen CS, Zhou C. Label-free evaluation of angiogenic sprouting in microengineered devices using ultrahigh-resolution optical coherence microscopy. J Biomed Opt. 2014; 19: 016006.

46. Li F, Song Y, Dryer A, Cogguillo W, Berdichevsky Y, Zhou C. Nondestructive evaluation of seizure-induced neuronal changes in organotypic rat hippocampal slice cultures using ultrahigh-resolution optical coherence microscopy. Neurophotonics. 2014; 1: 025002.

47. Belinson SE, Ledford K, Rasool N, Rollins A, Wilan N, Wang C, et al. Cervical epithelial brightness by optical coherence tomography can determine histological grades of cervical neoplasia. J Low Genit Tract Dis. 2013; 17: 160-6.

48. Gallwas J, Turk L, Friese K, Dannecker C. Optical coherence tomography as a non-invasive imaging technique for preinvasive and invasive neoplasia of the uterine cervix. Ultrasound Obstet Gynecol. 2010; 36: 624-9.

49. Gallwas J, Jalilova A, Ladurner R, Kolben TM, Kolben T, Ditsch N, et al. Detection of cervical intraepithelial neoplasia by using optical coherence tomography in combination with microscopy. J Biomed Opt. 2017; 22: 16013.

50. Zuluaga AF, Follen M, Boiko I, Malpica A, Richards-Kortum R. Optical coherence tomography: a pilot study of a new imaging technique for noninvasive examination of cervical tissue. Am J Obstet Gynecol. 2005; 193: 83-8.

51. Benoit a la Guillaume E, Martins F, Boccara C, Harms F. High-resolution handheld rigid endomicroscope based on full-field optical coherence tomography. J Biomed Opt. 2016; 21: 26005.

52. Carignan CS, Yagi Y. Optical endomicroscopy and the road to real-time, in vivo pathology: present and future. Diagn Pathol. 2012; 7: 98.